PAPER

CrossMark
click for updates

High nitrogen-content carbon nanosheets formed using the Schiff-base reaction in a molten salt medium as efficient anode materials for lithium-ion batteries†

Bin He, Wen-Cui Li and An-Hui Lu*

A series of porous carbon nanosheet materials with high nitrogen content have been prepared using melamine and terephthalaldehyde as carbon precursors through the Schiff-base reaction in a molten salt medium. The molten salt medium is responsible for the formation of sheet morphology and allows efficient immobilization of nitrogen atoms in the carbon framework during thermal pyrolysis, resulting in high-nitrogen-content carbons. XPS results demonstrate that, different from other reported carbons, the carbon nanosheets largely contain pyrrolic and pyridinic groups, both of which are very suitable for Li storage. When the carbon nanosheets are used as anode materials for lithium ion batteries (LIBs), they exhibit a high initial coulombic efficiency of *ca.* 63.1%, and a high and constant reversible capacity of 605 mA h g^{-1} at a current density of 100 mA g^{-1} even after 100 cycles. Moreover, they show a high-rate capability, *e.g.*, a high capacity of 199 mA h g^{-1} was obtained at 3000 mA g^{-1} (full charge within 4 min). In contrast, commercial graphite has a value less than 20 mA h g^{-1} at 3000 mA g^{-1}, showing one-tenth the capacity of the carbon nanosheet material. Such superior electrochemical performance is due to its high porosity, high nitrogen content of *ca.* 30 wt% and a unique two-dimensional (2D) structure. Thus, the proposed synthesis can be an alternative means for the preparation of high-nitrogen-content porous carbon with specific nitrogen species for energy storage applications.

Introduction

Lithium-ion batteries, which have been extensively used in various portable electronic devices and electric tools, have become one of the most popular power sources due to their high energy density and long cycle life.[1–4] However, the LIB anode has a low specific capacity and thus urgently requires improvement. Graphite is the most popular anode material in commercial LIBs owing to its high electrical conductivity and low cost, yet it has a low theoretical specific capacity (372 mA h g^{-1}) and lithium intercalation potential, which hinder its use for high power and large-scale energy storage.[5,6] Therefore, there is still a need to seek other high performance carbon materials. Although other alternative anode materials such as silicon,[7,8] metal alloys[9] and metal oxides[10–13] have been investigated because of their specific capacities that are theoretically several times higher, their cycle life is still limited by the serious pulverization of such anode materials during cycling and poor electronic conductivity.[14,15] When faced with the search for high

capacity and long-cycle-life anode materials, accompanied by a preference for materials with light weight, good electronic conductivity and flexibility, amorphous carbon materials have drawn much attention, due to their good chemical and thermal stability, and larger crystal lattice spacing allowing a higher lithium storage capability than graphite.[16–19] Moreover, the electrochemical performance of carbon can be further improved by tuning the electronic structure through doping N, B and O atoms into the carbon framework. Among these heteroatoms, nitrogen is very attractive because of its high electronegativity (nitrogen 3.5, carbon 3.0), small atomic diameter, and additional free electrons contributing to the conduction band of carbon.[20,21] In addition, the existence of nitrogen atoms also creates defects in carbon, generating more active sites for the lithium storage and movement involving the defects by the strong interaction between lithium and nitrogen-rich carbon.[22] In fact, our previous study has shown that nitrogen-doping can enhance the performance of LIBs.[11]

To date, various forms of carbon materials including carbon spheres,[23,24] carbon tubes,[25,26] carbon fibers,[27,28] and carbon nanosheets[29,30] have been prepared. In particular, sheet-like nanocarbons are very interesting for use as anodes of LIBs because of their large open flat structure, easily accessible pores and excellent electronic transport properties.[31,32] For example,

State Key Laboratory of Fine Chemicals, School of Chemical Engineering, Dalian University of Technology, Dalian 116024, P. R. China. E-mail: anhuilu@dlut.edu.cn; Fax: +86-411-84986112; Tel: +86-411-84986112

This journal is © The Royal Society of Chemistry 2015

J. Mater. Chem. A, 2015, 3, 579–585 | 579

Song and co-workers synthesized hierarchical porous carbon nanosheets exhibiting a favorable high-rate performance, for which the reversible capacities were 748 mA h g^{-1} at a current density of 20 mA g^{-1} and 460 mA h g^{-1} at 1000 mA g^{-1}.[33] However, the initial coulombic efficiency was only about 38.6% at 20 mA g^{-1}, which is rather low. Such a low initial coulombic efficiency reflects the fact that lithium ions are continually consumed in the cathode, leading to the loss of battery capacity and a low energy density.[34] A literature survey shows that in the case of amorphous carbons, their initial coulombic efficiencies are mostly in the range of 30–50% (for clarity, see Table S1, ESI†). This is due to the irreversible side reactions concentrated in the first electrochemical absorption of lithium ions, thus losing some irreversible lithium storage sites.[35,20] To improve energy density, research on porous carbon materials with a high initial coulombic efficiency is essential.

In view of the above, we here report a simple approach for the preparation of a new type of porous carbon with a nanosheet morphology, an amorphous framework, and a notably high nitrogen content up to 30 wt% with specific nitrogen species. When used as anode materials for LIBs, such a sheet-like structure facilitates fast diffusion and high conductivity of lithium ions, and consequently offers a high initial coulombic efficiency of ca. 63.1% and delivers a reversible capacity as high as 605 mA h g^{-1} at a current density of 100 mA g^{-1} after 100 cycles. This initial coulombic efficiency and reversible capacity are much higher than those of most reported amorphous porous carbons.

Experimental section

Synthesis of nitrogen-rich carbon nanosheets

Using a molten mixed salt method, carbon nanosheets were synthesized using melamine and terephthalaldehyde as carbon precursors. Typically, melamine and terephthalaldehyde were ground with 9.0 g LiCl–KCl (45/55 by weight) until a fine powder was obtained. Subsequently, the mixture was heated at 150 °C for 4 h, at 400 °C for 2 h and at 600 °C for 2 h in a tube furnace under a nitrogen atmosphere to obtain the carbon material. Next, the carbon material was immersed in deionized water to remove the salt. Three samples were prepared using this method with different molar ratios of terephthalaldehyde to melamine (T/M). The samples were denoted NC-1 with T/M = 1.0, NC-2 with T/M = 1.5 and NC-3 with T/M = 2.0. In order to clarify the role of the salt, a control sample was prepared with a molar ratio T/M of = 1.5 without using the salt, which was denoted as NC-4.

Characterization

The morphologies of the carbon samples were investigated by field-emission scanning electron microscopy (SEM) with a Hitachi S-4800I instrument at 10 kV. Nitrogen sorption isotherms were measured with a Micromeritics tristar 3000 instrument adsorption analyzer at 77 K. Before the measurements, the carbon samples were degassed under vacuum at 200 °C for 4 h until the pressure was below 0.05 mbar. The Brunauer–Emmett–Teller (BET) method was used to calculate the specific surface areas (S_{BET}). X-ray photoelectron spectroscopy (XPS) data were obtained with an ESCALAB250 electron spectrometer. Elemental analysis was performed on a CHNO elemental analyzer (Vario EL III, Elementar). X-ray diffraction (XRD) measurements were taken on a Rigaku D/Max 2400 diffractometer using Cu Kα radiation (40 kV, 100 mA, λ = 1.5406 Å). Raman spectra were collected on a homemade DL-2 microscopic Raman spectrometer, using the 244 or 532 nm line of a KIMMON laser. Thermogravimetric analysis was carried out from 40 to 800 °C at a heating rate of 10 °C min^{-1} under air flow, using an STA449 F3 Jupiter thermogravimetric analyzer (NETZSCH).

Electrochemical test

The working electrodes were prepared by mixing 80 wt% of the carbon sample, 10 wt% of conductive carbon black and 10 wt% of the polyvinylidene difluoride (PVDF) binder. Subsequently, the electrode slurry was coated onto rough copper foil, followed by dehydration at 100 °C for 12 h in a vacuum oven. Electrochemical measurements were carried out using a CR2025 coin-type cell with lithium metal as the counter electrode and a Celgard 2400 membrane as the separator. The graphite electrode consisting of commercial artificial graphite was prepared with the same weight ratio and steps. The electrolyte was 1 M LiPF$_6$ dissolved in a mixture of dimethyl carbonate (DMC), ethylmethyl carbonate (EMC), and ethylene carbonate (EC) (1 : 1 : 1 v/v/v) with 2 wt% fluorinated ethylene carbonate (FEC) as an additive. The cells were assembled in an argon-filled glovebox with water and oxygen concentrations under 1 ppm. Galvanostatic charge–discharge cycles were tested using a LAND CT2001A electrochemical workstation at various current densities between 0.005 and 3 V vs. Li$^+$/Li at room temperature. Electrochemical impedance spectroscopy (EIS) measurements were carried out before charge–discharge cycles in the frequency range of 100 kHz to 0.01 Hz with a zero-bias potential and 5 mV of amplitude.

Results and discussion

The synthesis strategy of the carbon nanosheet material is presented in Fig. 1. First, the Schiff-base reaction between melamine and terephthalaldehyde occurs at 150 °C in the presence of the LiCl–KCl mixed salt under an inert atmosphere, in which the amino groups of melamine react with the aldehyde groups of terephthalaldehyde to generate a polymer. Subsequently, the temperature gradually increases to the melting point of the salt, and the salt becomes a liquid. Meanwhile, the in situ generated Schiff-based polymer is gradually pyrolyzed in the molten salt medium to produce carbon. Finally, the carbon material is immersed in deionized water to remove the salt.

SEM characterization is used to investigate the morphologies of the samples. SEM images of NC-1, NC-2 and NC-3 with different ratios of terephthalaldehyde to melamine are shown in Fig. 2a–c, respectively. The three carbon samples are similar and consist of interconnected nanosheets. There is a small
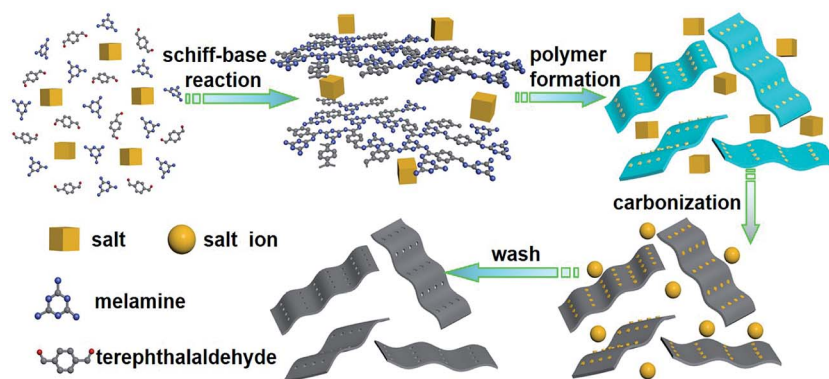
580 | J. Mater. Chem. A, 2015, 3, 579–585

This journal is © The Royal Society of Chemistry 2015

Fig. 1 Illustration of the preparation strategy of carbon nanosheets.
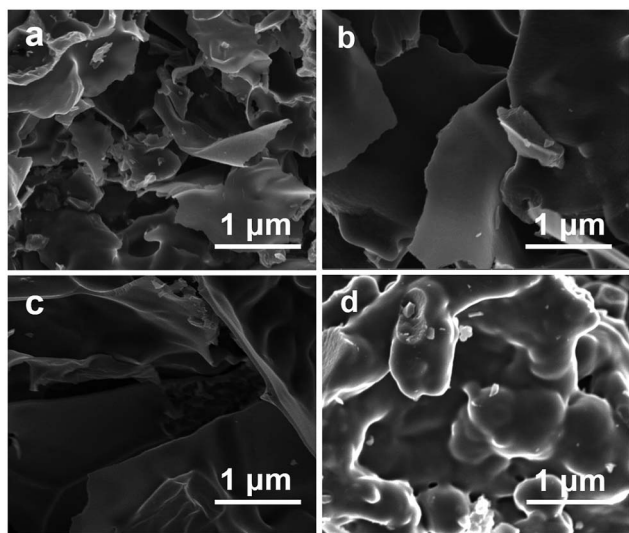

Fig. 2 The SEM images of (a) NC-1, (b) NC-2, (c) NC-3 and (d) NC-4.

difference between them caused by the degree of crosslinking, which is relative to the number of amino and aldehyde groups. Hence, the SEM observation clearly shows that the carbons synthesized in the molten salt medium have a sheet-like nanostructure. Such nanosheet materials are very different from carbons produced using hydrothermal or ionothermal methods, which are often particulate powders, hierarchical structures or carbon spheres. To investigate the influence of the molten salt on the formation of the 2D carbon nanosheets, we have used SEM characterization of the sample prepared without adding salt. It is clear from Fig. 2d that the carbonization product (NC-4) only consists of dense blocks and no sheet-shaped nanostructures can be found. This result further indicates that the salt plays an important role in the formation of nanosheets. We presumably believe that the molten salt can create an ionized environment that can dissolve polar intermediates of the polymer derived from terephthalaldehyde and melamine, and prevent the product from forming agglomerations due to the high viscosity of the molten salt. In contrast, under hydrothermal or ionothermal conditions, formation of spherical carbons by minimizing their surface energy is a

common phenomenon that is probably attributed to the hydrophobic property of the carbons and the low viscosity of the used solvents allowing easy agglomeration of the generated carbon species.[36]

Nitrogen sorption isotherms of the carbon samples are shown in Fig. S1,† and the structural parameters (S_{BET}, V_{total} and V_{micro}) are listed in Table 1. The isotherms of NC-1 and NC-3 are of type IV with a clear hysteresis loop in the relative pressure range of 0.4–0.8, demonstrating mesoporous characteristics. The isotherms of NC-2 and NC-4, however, are of type I, indicating microporous characteristics. As can be seen, there is at least a tenfold increase in the specific surface area for all of the carbons derived from the molten salt system compared with that of the sample prepared without it. The maximum specific surface area of 696 m^2 g^{-1} was observed for sample NC-2 and was almost twenty times (31 m^2 g^{-1}) that of the sample prepared without the salt medium. On the basis of the above results, we can speculate that the salt is the key factor in improving the specific surface area, possibly as a porogen and reaction medium,[37,38] which can then be easily removed by deionized water. Meanwhile, the mole ratio of terephthalaldehyde to melamine affects the specific surface area as shown in Table 1. The surface areas are quite different, which may be caused by the rate and the degree of polymerization.

X-ray photoelectron spectroscopy (XPS) is used to estimate the contents and the chemical states of the carbon and nitrogen atoms in the samples. The full scan XPS of the four samples (ESI, Fig. S2†) has three peaks centered at binding energies of

Table 1 Structural parameters of the carbon samples

Samples	S_{BET}[a]/m^2 g^{-1}	V_{total}[b]/cm^3 g^{-1}	V_{micro}[c]/cm^3 g^{-1}
NC-1	586	0.39	0.19
NC-2	696	0.37	0.31
NC-3	332	0.21	0.14
NC-4	31	0.02	0.02

[a] Specific surface area calculated using the BET equation in the relative pressure range of 0.05–0.25. [b] Single point pore volume from adsorption isotherms at $P/P_0 = 0.97$. [c] Micropore volume calculated using the t-plot method.

ca. 284.6 eV, 398.2 eV and 531.9 eV, corresponding to C 1s, N 1s and O 1s, respectively. Fig. 3 shows the N 1s spectra of the four samples, which can be well-fitted to two peaks with binding energies of 398.1 and 399.8 eV for NC-1 (Fig. 3a), 398.1 and 399.7 eV for NC-2 (Fig. 3b), 398.1 and 399.9 eV for NC-3 (Fig. 3c) and 398.0 and 399.8 eV for NC-4 (Fig. 3d), representing pyridinic N (N-6 at 398.0 ± 0.2 eV), pyrrolic or pyridonic N (N-5 at 399.7 ± 0.2 eV).[39] The pyridinic nitrogen atom is located at the edges of the carbon nanosheets. It is formed by substituting a carbon atom on the C_6 ring by a nitrogen atom and bonding with two sp^2 carbon atoms which contributes one pair of lone electrons. The pyrrolic nitrogen is a nitrogen atom on a five-membered ring and contributes two electrons to the system.[39] In addition, there is no peak associated with oxidized nitrogen, which would appear at 402–405 eV,[21] suggesting that the oxygen atoms in the four samples are bonded to the carbon atoms. Compared with the other nitrogen-doped carbons, our work provides a simple route to produce a high nitrogen content, porous and amorphous carbon with specific nitrogen species, which largely has two species of nitrogen. Interestingly, the nitrogen species of the carbons are almost identical, although these samples were prepared at the same pyrolysis temperature, however using different mole ratios of terephthalaldehyde to melamine.

The results of elemental analysis and fitting of the N 1s spectra to the carbon materials are listed in Table 2. Clearly, the nitrogen contents in the carbon materials are affected by the melamine concentration and synthesis conditions. It is understandable that the nitrogen content increases as the concentration of melamine increases from 33.3% to 50%, caused by the high nitrogen content (~67%) in melamine. As the mole ratio of terephthalaldehyde to melamine reaches 1.0, the nitrogen content is 30.51 wt%, much higher than in other nitrogen-rich carbon materials of carbon nanofiber webs used

Table 2 Elemental analysis of the carbon samples

	Elemental analysis[a] (wt%)				XPS[c] (atom%)			% of total N 1s	
	C	H	N	O[b]	C	N	O	N-5	N-6
NC-1	54.85	1.86	30.51	12.78	68.18	22.67	9.15	46.62	53.38
NC-2	51.67	2.08	29.20	17.05	74.58	19.90	5.52	43.66	56.34
NC-3	63.24	2.05	22.29	12.42	78.81	15.14	6.05	48.05	51.95
NC-4	66.61	2.22	21.34	9.83	81.56	8.49	9.95	43.26	56.74

[a] The C, H, N contents were directly measured by elemental analysis. [b] Calculated by difference. [c] Weight percentage of C, N and O elements obtained from XPS analysis.

for energy storage which have nitrogen contents 10.25 wt% (ref. 40) and 15.01 wt%.[41] Comparing samples NC-2 and NC-4, which are synthesized by different methods but with the same mole ratio of terephthalaldehyde to melamine, it can be seen that the nitrogen content in sample NC-2 is much higher than in NC-4. What is more, the nitrogen contents in NC-1 and NC-3 are also higher than in NC-4. Thus, the higher nitrogen content verifies the fact that the molten salt helps to immobilize the nitrogen and reduce its loss. It may be that the K^+ or Li^+ in the molten salt medium will attract the pair of electrons of the nitrogen atom and then slow the loss of nitrogen during carbonization, which can be seen from the XPS results. The contents of pyridinic and pyrrolic nitrogen both of which contain one pair of lone electrons are much higher in NC-1, NC-2 and NC-3 than in NC-4. The above result indicates that our work provides a simple route to produce porous and amorphous carbon nanosheet materials with high nitrogen content.

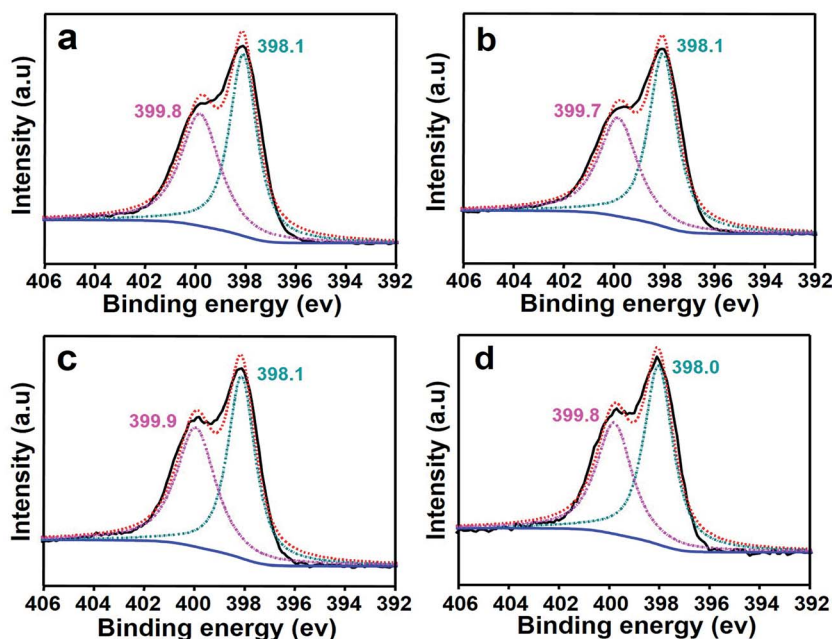The wide angle XRD patterns of NC-2 and NC-4 materials synthesized by different methods are shown in Fig. 4a. NC-4

Fig. 3 XPS N 1s spectra of (a) NC-1, (b) NC-2, (c) NC-3 and (d) NC-4.

shows a strong wide diffraction peak at 24.8° and a peak at 43.1°, which are attributed to the (002) and (100) planes of graphite, respectively. While NC-2 shows a relatively wide (002) peak at 25.6°, the (100) diffraction peak has disappeared. According to Bragg's law, the interplanar spacings (d_{002}) of NC-2 and NC-4 are 3.48 Å and 3.59 Å respectively, both of which are larger than that (3.35 Å) of bulk graphite. In general, a larger interplanar spacing is better for lithium insertion/extraction, while too large an interplanar spacing will weaken the bond to lithium ions, leading to a low specific capacity. Additionally, the intensity of the two peaks in NC-4 is stronger than in NC-2, implying a higher degree of order in NC-4. The structural difference between NC-2 and NC-4 was further demonstrated by Raman spectroscopy.

In Fig. 4b, Raman spectra show typical characteristic D- and G-bands of disordered graphitic materials, located at *ca.* 1360 and 1590 cm^{-1}, respectively. The intensity ratios of the D-band to the G-band (I_D/I_G) of NC-2 and NC-4 are 2.09 and 1.57 respectively, suggesting that there are more defects in NC-2.[30,42] In addition to defects, this may be also due to the influence of the nitrogen-doping spoiling the local symmetry and contributing to the D-band intensity.[43] Thus, from XRD and Raman results, it can be concluded that NC-2 has more defects, which can serve as additional active sites for Li storage.

As mentioned earlier, nitrogen-doping in the carbon structure can create a significant number of defects which may serve as additional active sites for Li storage, and the sheet structure may facilitate fast diffusion of lithium ions. Therefore, the carbon samples were further investigated as anode materials for lithium ion batteries in a half-cell configuration. The electrochemical performance of these carbons is presented in Fig. 5. The first galvanostatic charge–discharge profiles of the carbon under a current density of 100 mA g^{-1} are shown in Fig. 5a. As seen, the carbon nanosheets deliver higher reversible capacity, which increases from 496.1 mA h g^{-1} for NC-4 to 622.8 mA h g^{-1} for NC-2 with a corresponding increase of the specific surface area from 31 m^2 g^{-1} to 696 m^2 g^{-1}. These results suggest that the abundant porosity, high surface area and 2D nanosheet structure are beneficial for enhanced lithium storage and charge transfer. Fig. 5b shows the cycling performance of carbon samples at 100 mA g^{-1} in the voltage range of 0.005–3 V. It can be seen that the carbon samples synthesized in the molten salt medium show excellent cycle stability with high capacity. After 100 cycles, NC-1, NC-2, and NC-3 demonstrate reversible capacities of 479.7, 605.3, and 398.0 mA h g^{-1} respectively, which are remarkably larger than that of the theoretical capacity of graphite (~372 mA h g^{-1}). In contrast, NC-4 synthesized without the salt delivers a much lower reversible capacity of *ca.* 236.8 mA h g^{-1} after 100 cycles and worse cycle stability than samples synthesized in the molten salt medium. The results indicate that the carbon nanosheet materials possess superior lithium storage ability and
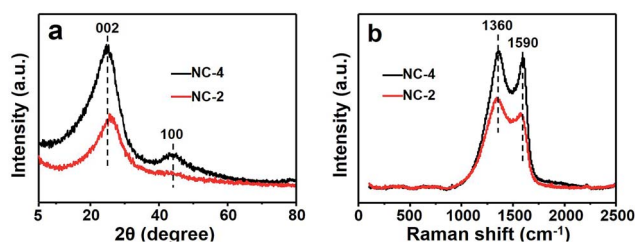

Fig. 4 (a) Wide-angle powder XRD patterns and (b) Raman spectra of NC-2 and NC-4.
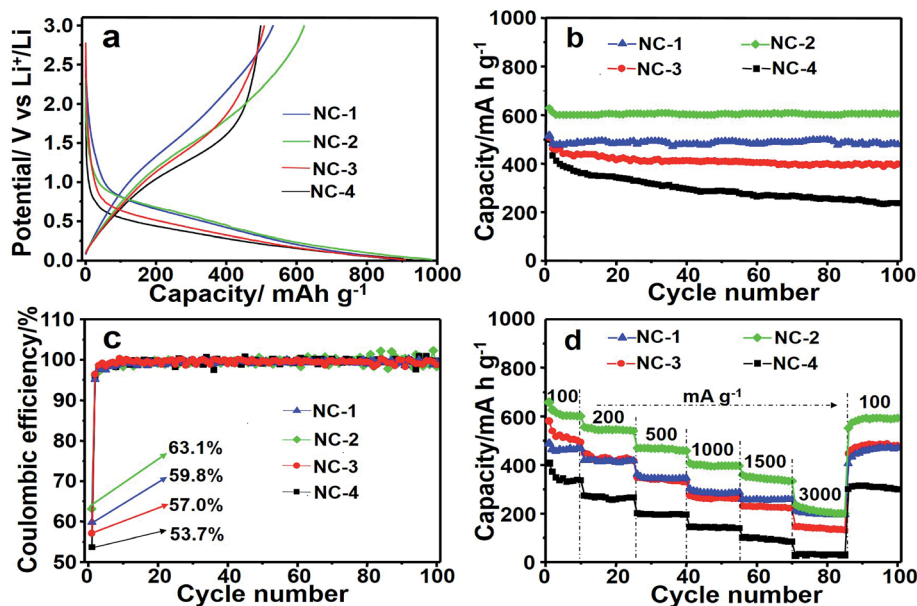

Fig. 5 Electrochemical performance of NC-1, NC-2, NC-3 and NC-4: (a) the first charge–discharge profiles at a current density of 100 mA g^{-1}, (b) cycle performance in the range of 0.005–3 V, (c) coulombic efficiencies and (d) rate performance at different current densities from 100 to 3000 mA g^{-1}.

This journal is © The Royal Society of Chemistry 2015

J. Mater. Chem. A, 2015, **3**, 579–585 | **583**

outstanding cycling stability, which could be attributed to the defects induced by nitrogen-doping, large porosity as well as the 2D nanosheet structure. The N-doping process creates defects in the carbon, which generate more active sites for the lithium storage and facilitate the penetration of lithium through the defects by the strong interaction between lithium and nitrogen-rich carbons. More importantly, previous theoretical study has demonstrated that two such nitrogen species of pyridinic and pyrrolic structures are beneficial in anode materials for lithium ion batteries.[44] As shown in Fig. 5c, the initial coulombic efficiency of the NC-2 sample is as high as 63.1%, which is the highest among the samples, followed by NC-1 (59.8%), NC-3 (57.0%), and NC-4 (53.7%).

It should be noted that the initial coulombic efficiency of NC-2 is higher than for some reported amorphous carbons.[45,46] In addition, the coulombic efficiency of NC-2 quickly increases to nearly 100% after several cycles, suggesting that the N functionalities and nanosheet structure can improve the coulombic efficiency to some extent. The fact that NC-2 shows a higher initial coulombic efficiency may be due to the small amount of Li ion residues in the carbon nanosheets, which are hardly washed away by water (ESI, Fig. S3†), that provide an extra Li source for reducing the first-cycle irreversible capacity.[47]

The anodes made from the carbon nanosheet material show excellent rate performance (Fig. 5d). For testing, all cells were cycled at a rate of 100 mA g^{-1} for 10 cycles, and then at various current densities from 200 to 3000 mA g^{-1} each for 15 cycles. It can be seen that NC-2 exhibits the best performance, and its reversible capacity is stabilized at *ca.* 600.3 mA h g^{-1} after 10 cycles at a rate of 100 mA g^{-1}. Further cycling at different current densities shows reversible charge capacities of 536.0, 430.0, 396.1, 334.1 and 199.2 mA h g^{-1} at 200, 500, 1000, 2000 and 3000 mA g^{-1} respectively. When the current density is set back to 100 mA g^{-1} after cycling at different rates, the specific capacity can be recovered to 593.2 mA h g^{-1}, indicating very stable cycling performance. Indeed, the value for commercial natural graphite remains less than 20 mA h g^{-1} at 3000 mA g^{-1} (ESI, Fig. S4†), showing one-tenth the capacity of the carbon nanosheet material. In addition, the carbon nanosheet samples NC-1 and NC-3 also show good rate performance with discharge capacities of 195.9 mA h g^{-1} and 133.4 mA h g^{-1} at 3000 mA g^{-1}. In contrast, NC-4 displays the lowest rate performance with a discharge capacity of 30.0 mA h g^{-1} at 3000 mA g^{-1}, which verifies the fact that the 2D nanosheet structure has a much shorter lithium-ion diffusion path which is beneficial for fast and effective lithium-ion insertion/extraction and thus results in an improved rate performance over the 3D carbon block. Moreover, the higher specific surface area of the carbon nanosheets is also responsible for the outstanding performance because the porous nanostructure can shorten the transport length for Li$^+$ ions and offer a large electrode/electrolyte interface for the charge transfer reaction. In comparison with the recent reports on amorphous and crystalline carbon-based anode materials (for details, see Table S1†), sample NC-2 shows outstanding rate capability and a high initial coulombic efficiency. This remarkably improved electrochemical performance can be attributed to a high nitrogen content with pyridinic and pyrrolic nitrogen and a high specific surface area as well as a unique 2D nanosheet structure.

To further understand the good performance of NC-2, EIS measurements were carried out to verify the kinetics of Li-ion insertion. The electrochemical impedance spectra of NC-2 and NC-4 are shown in Fig. S5a and b.† The Nyquist plots are similar in shape, consisting of one depressed semicircle in the high-to-medium frequency region and an inclined line at low frequency, which can be ascribed to the charge-transfer resistance and Warburg impedance.[17,48] Generally, the numerical value of the diameter of the semicircle on the Z' axis is approximately equal to the charge transfer resistance, while the lithium ion diffusion coefficient of the electrode is proportional to the slope values of the inclined line at low frequency.[49] It should be noted that the intercalation and deintercalation of the lithium ions are usually determined by the charge-transfer resistance.[50] Apparently, sample NC-2 shows a smaller semicircle diameter than NC-4. This shows that NC-2 possesses a lower charge transfer resistance compared to NC-4, indicating that it exhibits faster Li-ion insertion kinetics. These results further confirmed that the 2D nanosheet structure and high surface area are favorable for lithium-ion insertion/extraction as well as the charge transfer reaction.

Conclusions

Two-dimensional carbon nanosheet materials with different nitrogen-contents were synthesized by a simple method in a molten salt medium using melamine and terephthalaldehyde as precursors with the potential for large scale production. Their large surface area, high nitrogen content of *ca.* 30 wt% and 2D nanosheet structure are not only very favorable for the fast and steady transfer of electrons and ions, but also offer more active sites for lithium storage. For this reason, anodes made from the carbon nanosheet materials exhibit high specific capacity and good rate performance, especially for sample NC-2 which has a reversible capacity of up to 605.3 mA h g^{-1} at a current density of 100 mA g^{-1} after 100 cycles and rate capacities of 600.3, 536.0, 430.0, 396.0, 334.0 and 199.2 mA h g^{-1} at 100, 200, 500, 1000, 2000 and 3000 mA g^{-1} respectively. Thus a lithium cell made using the carbon nanosheet material can be charged and discharged at high currents (3000 mA g^{-1}) in a very short time of only a few minutes, showing one third of the capacity at low currents (100 mA g^{-1}). Moreover, these carbon nanosheet materials with very high nitrogen content offer great potential in other applications, such as supercapacitors and catalysis.

Acknowledgements

References

1 I. Mochida, C. H. Ku and Y. Korai, *Carbon*, 2001, **39**, 399–410.

584 | *J. Mater. Chem. A*, 2015, **3**, 579–585

This journal is © The Royal Society of Chemistry 2015

2 H. Li, Z. X. Wang, L. Q. Chen and X. J. Huang, *Adv. Mater.*, 2009, **21**, 4593–4607.

3 Y. G. Guo, J. S. Hu and L. J. Wan, *Adv. Mater.*, 2008, **20**, 2878–2887.

4 M. Wakihara, *Mater. Sci. Eng., R*, 2001, **33**, 109–134.

5 J. B. Goodenough and Y. Kim, *Chem. Mater.*, 2010, **22**, 587–603.

6 S. R. Mukai, T. Hasegawa, M. Takagi and H. Tamon, *Carbon*, 2004, **42**, 837–842.

7 A. M. Chockla, J. T. Harris, V. A. Akhavan, T. D. Bogart, V. C. Holmberg, C. Steinhagen, C. B. Mullins, K. J. Stevenson and B. A. Korgel, *J. Am. Chem. Soc.*, 2011, **133**, 20914–20921.

8 H. Wu and Y. Cui, *Nano Today*, 2012, **7**, 414–429.

9 K. Zhuo, M. G. Jeong and C. H. Chung, *J. Power Sources*, 2013, **244**, 601–605.

10 F. Han, D. Li, W. C. Li, C. Lei, Q. Sun and A. H. Lu, *Adv. Funct. Mater.*, 2013, **23**, 1692–1700.

11 C. Lei, F. Han, D. Li, W. C. Li, Q. Sun, X. Q. Zhang and A. H. Lu, *Nanoscale*, 2013, **5**, 1168–1175.

12 F. Han, W. C. Li, M. R. Li and A. H. Lu, *J. Mater. Chem.*, 2012, **22**, 9645–9651.

13 C. Lei, F. Han, Q. Sun, W. C. Li and A. H. Lu, *Chem.–Eur. J.*, 2013, **19**, 1–8.

14 M. Winter and J. O. Besenhard, *Electrochim. Acta*, 1999, **45**, 31–50.

15 M. S. Wang and L. Z. Fan, *J. Power Sources*, 2013, **244**, 570–574.

16 F. Bonino, S. Brutti, P. Reale, B. Scrosati, L. Gherghel, J. Wu and K. Mullen, *Adv. Mater.*, 2005, **17**, 743–746.

17 G. P. Hao, F. Han, D. C. Guo, R. J. Fan, G. Xiong, W. C. Li and A. H. Lu, *J. Phys. Chem. C*, 2012, **116**, 10303–10311.

18 W. Xing, J. S. Xue and J. R. Dahn, *J. Electrochem. Soc.*, 1996, **143**, 3046–3052.

19 Q. Sun, X. Q. Zhang, F. Han, W. C. Li and A. H. Lu, *J. Mater. Chem.*, 2012, **22**, 17049–17054.

20 B. Guo, X. G. Sun, G. M. Veith, Z. H. Bi, S. M. Mahurin, C. Liao, C. Bridges, M. P. Paranthaman and S. Dai, *Adv. Energy Mater.*, 2013, **3**, 708–712.

21 Y. Mao, H. Duan, B. Xu, L. Zhang, Y. S. Hu, C. C. Zhao, Z. X. Wang, L. Q. Chen and Y. S. Yang, *Energy Environ. Sci.*, 2012, **5**, 7950–7955.

22 Z. Li, Z. W. Xu, X. H. Tan, H. L. Wang, C. M. B. Holt, T. Stephenson, B. C. Olsen and D. Mitlin, *Energy Environ. Sci.*, 2013, **6**, 871–878.

23 S. Wang, W. C. Li, G. P. Hao, Y. Hao, Q. Sun, X. Q. Zhang and A. H. Lu, *J. Am. Chem. Soc.*, 2011, **133**, 15304–15307.

24 G. H. Wang, Q. Sun, R. Zhang, W. C. Li, X. Q. Zhang and A. H. Lu, *Chem. Mater.*, 2011, **23**, 4537–4542.

25 C. C. Su and S. H. Chang, *Carbon*, 2011, **49**, 5271–5282.

26 W. H. Shin, H. M. Jeong, B. G. Kim, J. K. Kang and J. W. Choi, *Nano Lett.*, 2012, **12**, 2283–2288.

27 X. Q. Zhang, Q. Sun, W. Dong, D. Li, A. H. Lu, J. Q. Mu and W. C. Li, *J. Mater. Chem. A*, 2013, **1**, 9449–9455.

28 C. Kim, K. S. Yang, M. Kojima, K. Yoshida, Y. J. Kim, Y. A. Kim and M. Endo, *Adv. Funct. Mater.*, 2006, **16**, 2393–2397.

29 Y. Fang, Y. Y. Lv, R. C. Che, H. Y. Wu, X. H. Zhang, D. Gu, G. F. Zheng and D. Y. Zhao, *J. Am. Chem. Soc.*, 2013, **135**(4), 1524–1530.

30 H. Wang, C. J. Zhang, Z. H. Liu, L. Wang, P. X. Han, H. X. Xu, K. Zhang, H. M. Dong, J. H. Yao and G. L. Cui, *J. Mater. Chem.*, 2011, **21**, 5430–5434.

31 L. Chen, Z. Y. Wang, C. N. He, N. Q. Zhao, C. S. Shi, E. Z. Liu and J. J. Li, *ACS Appl. Mater. Interfaces*, 2013, **5**, 9537–9545.

32 Z. J. Fan, Y. Liu, J. Yan, G. Q. Ning, Q. Wang, T. Wei, L. J. Zhi and F. Wei, *Adv. Energy Mater.*, 2012, **2**, 419–424.

33 R. R. Song, H. H. Song, J. S. Zhou, X. H. Chen, B. Wu and H. Y. Yang, *J. Mater. Chem.*, 2012, **22**, 12369–12374.

34 S. Flandrois and B. Simon, *Carbon*, 1999, **37**, 165–180.

35 Y. S. Hu, P. Adelhelm, B. M. Smarsly, S. Hore, M. Antonietti and J. Maier, *Adv. Funct. Mater.*, 2007, **17**, 1873–1878.

36 J. Liu, T. Y. Yang, D. W. Wang, G. Q. Lu, D. Y. Zhao and S. Z. Qiao, *Nat. Commun.*, 2013, **4**, 2798.

37 B. C. Jang, M. Y. Park, O. B. Chae, S. J. Park, Y. J. Kim, S. M. Oh, Y. Z. Piao and T. H. Hyeon, *J. Am. Chem. Soc.*, 2012, **134**, 15010–15015.

38 N. Fechler, T. P. Fellinger and M. Antonietti, *Adv. Mater.*, 2013, **25**, 75–79.

39 C. O. Ania, V. Khomenko, E. R. Pinero, J. B. Parra and F. Beguin, *Adv. Funct. Mater.*, 2007, **17**, 1828–1836.

40 L. Qie, W. M. Chen, Z. H. Wang, Q. G. Shao, X. Li, L. X. Yuan, X. L. Hu, W. X. Zhang and Y. H. Huang, *Adv. Mater.*, 2012, **24**, 2047–2050.

41 Z. H. Wang, X. Q. Xiong, L. Qie and Y. H. Huang, *Electrochim. Acta*, 2013, **106**, 320–326.

42 Z. J. Fan, J. Yan, G. Q. Ning, T. Wei, L. J. Zhi and F. Wei, *Carbon*, 2013, **60**, 538–561.

43 H. C. Chen, F. G. Sun, J. T. Wang, W. C. Li, W. M. Qiao, L. C. Ling and D. H. Long, *J. Phys. Chem. C*, 2013, **117**, 8318–8328.

44 C. C. Ma, X. H. Shao and D. P. Cao, *J. Mater. Chem.*, 2012, **22**, 8911–8915.

45 Q. T. Zhang, H. X. Sun, X. M. Wang, Z. Q. Zhu, W. D. Liang, A. Li, S. H. Wen and W. Q. Deng, *Energy Technol.*, 2013, **1**, 721–725.

46 J. L. Li, R. M. Yao, J. Bai and C. B. Cao, *ChemPlusChem*, 2013, **78**, 797–800.

47 Z. S. Wu, L. L. Xue, W. C. Ren, F. Li, L. Wen and H. M. Cheng, *Adv. Funct. Mater.*, 2012, **22**, 3290–3297.

48 F. Y. Cheng, H. B. Wang, Z. Q. Zhu, Y. Wang, T. R. Zhang, Z. L. Tao and J. Chen, *Energy Environ. Sci.*, 2011, **4**, 3668–3675.

49 C. G. Hu, Y. Xiao, Y. Zhao, N. Chen, Z. P. Zhang, M. H. Cao and L. T. Qu, *Nanoscale*, 2013, **5**, 2726–2733.

50 H. W. Ha, N. J. Yun and K. Kim, *Electrochim. Acta*, 2007, **52**, 3236–3241.